Published in final edited form as:

Nat Photonics. 2018 September ; 12(9): 540–547. doi:10.1038/s41566-018-0224-2.

Nano-optic endoscope for high-resolution optical coherence tomography *in vivo*

Hamid Pahlevaninezhad[1,2,†], **Mohammadreza Khorasaninejad**[2,†], **Yao-Wei Huang**[2,3,†], **Zhujun Shi**[4], **Lida P. Hariri**[1], **David C. Adams**[1], **Vivien Ding**[2,5], **Alexander Zhu**[2], **Cheng-Wei Qiu**[3], **Federico Capasso**[2,*], and **Melissa J. Suter**[1,*]

[1]Harvard Medical School and Massachusetts General Hospital, Boston MA 02114, United States

[2]John A. Paulson School of Engineering and Applied Science, Harvard University, Cambridge MA 02138, United States

[3]Department of Electrical and Computer Engineering, National University of Singapore, 117583 Singapore, Singapore

[4]Department of Physics, Harvard University, Cambridge, MA 02138, United States

[5]Department of Electrical and Computer Engineering, University of Waterloo, Waterloo Ontario N2L 3G1, Canada

Abstract

Acquisition of high-resolution images from within internal organs using endoscopic optical imaging has numerous clinical applications. However, difficulties associated with optical aberrations and the trade-off between transverse resolution and depth-of-focus significantly limit the scope of applications. Here, we integrate a metalens, with the ability to modify the phase of incident light at sub-wavelength level, into the design of an endoscopic optical coherence tomography catheter (termed nano-optic endoscope) to achieve near diffraction-limited imaging through negating non-chromatic aberrations. Remarkably, the tailored chromatic dispersion of the metalens in the context of spectral interferometry is utilized to maintain high-resolution imaging beyond the input field Rayleigh range, easing the trade-off between transverse resolution and depth-of-focus. We demonstrate endoscopic imaging both in resected human lung specimens and in sheep airways *in vivo*. The combination of the superior resolution and higher imaging depth-of-

*Corresponding author: capasso@seas.harvard.edu, msuter@mgh.harvard.edu.
†These authors contributed equally to this work.
Correspondence and requests for materials should be addressed to MJS.

Author contributions. HP, MK, and YWH carried out analyses, fabricated endoscopes, and planned and executed the experiments. ZS performed computational analysis for metalens design. LPH, MJS, and HP performed the ex vivo and in vivo imaging. MJS and DCA implemented the OCT system. HP and DCA processed imaging data. VD and AZ assisted with experiment and fabrication. HP prepared the original manuscript with significant contributions from MK, YWH, and CWQ. MJS and FC supervised the project and participated in manuscript preparation.

Competing financial interests. HP, MK, YWH, ZS, MJS, and FC are the inventors on a relevant provisional patent application (application number: 62598455) owned by Harvard University and Massachusetts General Hospital.

Supplementary information is available for this paper at

focus of the nano-optic endoscope will likely increase the clinical utility of endoscopic optical imaging.

Endoscopic optical imaging using fiber optic catheters has provided numerous opportunities for obtaining information from remote, hard-to-reach places with several applications including medical imaging. In particular, endoscopic optical coherence tomography (OCT)[1,2], capable of providing detailed images of tissue microstructure millimeters deep into the tissue, is emerging as a promising tool for detection, diagnosis, and monitoring of disease in luminal organs such as the coronary arteries[3–5], the gastrointestinal tract[6,7], and the pulmonary airways[8,9]. However, despite pressing clinical needs for tools and instruments capable of accurately visualizing pathology including the extension of lesions in luminal organs, volumetric endoscopic optical imaging techniques have not been translated into routine clinical practice in many applications. A likely reason for this, amongst others, is the shortcomings associated with each technique. Some imaging modalities such as confocal endomicroscopy provide sufficient resolution to visualize tissue structures even at cellular levels but lack adequate penetration depth and field-of-view necessary for impact in many clinical applications. Others like conventional OCT provide increased depth range and field-of-view but fall short of desired resolution. Difficulties associated with optical aberrations and the trade-off between the transverse resolution and the depth-of-focus continue to plague clinical adoption.

OCT was originally developed based on low-coherence interferometry[10,11] to acquire images of optical scattering from sub-surface tissue structures by measuring the cross-correlation function[12,13]. Demands for high-speed acquisition crucial to wide-field imaging of luminal organs led to the advent of Fourier–domain techniques[14–18] that measure the spectral density function to obtain a depth-resolved line profile of tissue through Fourier transformation with significantly improved sensitivity. In practice, the spectral density function is measured using either a broadband light source-interferometer-spectrometer configuration or a wavelength-swept light source-interferometer-fast detector configuration.

Increasing the resolution of OCT systems has been recently the subject of intense research[19–26]. This is typically achieved by using light sources with shorter wavelengths with broader bandwidths to improve axial and lateral resolution. However, aside from technical difficulties associated with these systems, a fundamental limitation is the greatly increased scattering at shorter wavelengths that severely limits light penetration and, in turn, imaging depth in tissue[20,21].

Another important concern is that imaging with high lateral resolution by tightly focusing the illumination light greatly reduces the depth-of-focus, leading to the maintenance of high lateral resolution imaging for only very short depth range. Different approaches have been proposed for the extension of depth-of-focus in the endoscopic settings including illumination with multiple beams of different focal lengths using a combination of multiple fibers and a complex arrangement of miniature optical lenses[27] and addition of annular amplitude and/or phase filters to generate axially elongated illumination beams[23,24]. These techniques, however, result in reduced sensitivity and a compromise in lateral resolution due to the presence of side lobes. In addition, diffraction-limited imaging cannot be reached with

these techniques due to spherical aberration and astigmatism (resulting from azimuthal symmetry of the focusing elements and the filters together with asymmetrical curvatures of the protective layers in the optical path).

Aside from aforementioned modifications and others[28,29], OCT catheters typically utilize the same basic principle. The optical field delivered through a length of single-mode fiber to the distal end of the catheter is redirected and focused into the tissue using either a graded-index (GRIN) lens-prism configuration[1] (Figure 1a) or an angle-polished ball lens[30] (Figure 1b). This optical assembly is encased inside a stationary transparent protective sheath. Images are captured by helically scanning the optical beam within the tissue lumen using distal or proximal actuators. Although, the simplicity of the basic design has allowed these catheters to be utilized in numerous clinical applications, there are several shortcomings. Constraints in the shape of ball lenses (fabrication of a miniature lens with arbitrary shape is difficult) and the index profile of GRIN lenses (typical manufacturing techniques[31] only allow azimuthally-symmetric near quadratic index profile with small refractive index contrasts) result in spherical aberrations and thus deviate from diffraction-limited focusing. In addition, the presence of multilayered structures in the optical path from the fiber facet to the focal point degrades the focusing quality. For example, the protective sheath introduces significant astigmatism owing to the different curvatures parallel and perpendicular to the catheter axis. Furthermore, optical properties of the output beam such as chromatic dispersion and polarization states cannot be modified. These significant limitations cannot be rectified in the current OCT catheter designs as the shape and refractive index profile of the focusing elements are not readily adjustable.

Here, we introduce a new class of fiber optic catheters using metalenses[32,33] that consist of arrays of subwavelength-spaced scatterers at an interface. Based on their geometric parameters and distribution, these optical scatterers locally shift the phase of the incident light and shape its wavefront, enabling realization of a wide variety of planar optical devices such as metalenses[34] and holograms[35,36]. The ability to tailor the phase at will with high spatial resolution allows metalenses to be free of spherical aberration and astigmatism, overcoming the essential barriers to diffraction-limited focusing and imaging. Notably, this technique can be used to achieve high-quality focusing in any complex medium with arbitrary refractive index profile and geometry. We integrate a metalens into the design of an endoscopic OCT catheter (termed nano-optic endoscope, Figure 1c) and demonstrate high-resolution imaging at extended depth-of-focus with no requirements for additional acquisition/processing time[37] or complex arrangements of optical elements[27]. Crucially, the tailored chromatic dispersion of the metalens in the context of spectral interferometry allows for the maintenance of high-resolution imaging significantly beyond the Rayleigh range of the incident light. We compare the nano-optic endoscope to a commercial GRIN lens catheter and a ball lens catheter to assess output beam quality and to highlight the superior performance of the former. The ability of the nano-optic endoscope to obtain high-resolution images of sub-surface tissue structures *in vivo* will likely increase the clinical utility of OCT in detection, diagnosis, and monitoring of diseases.

Nano-optic endoscope design and fabrication

A schematic of the nano-optic endoscope is depicted in Figure 2a. Light is delivered and subsequently collected through a length of single mode fiber housed within a drive cable and a ferrule with an 8° angle-polished end facet to reduce reflections. A prism attached to the ferrule redirects the light towards the metalens, for a side-viewing catheter suitable for imaging luminal organs. The transmissive metalens comprised of amorphous silicon (a-Si) nanopillars on a 170 μm-thick cover glass focuses and collects light to and from a target object (e.g. tissue). Figure 2b shows a photographic image of the fabricated nano-optic endoscope. The optical components at the distal end of the catheter were assembled using a custom-built platform comprised of holders for the metalens, fiber, and prism mounted on separate translational and rotational stages to ensure accurate alignment. The components were bonded using optical adhesive during simultaneous monitoring of the output beam to ensure the optimal performance. A glass capsule surrounds the distal end of the optical core to prevent direct contact of the rotating probe from the tissue being imaged to protect the distal optics from contamination. The protective sheath is known to introduce aberrations including astigmatism owing to its different curvatures parallel and perpendicular to the endoscope axis. This is a common issue of the standard OCT catheters.

We designed the metalens to focus light from the fiber facet (considered as a point source) located at (x_s, y_s, z_s) into a diffraction-limited spot at (x_f, y_f, z_f) free from spherical aberrations and astigmatism. To accomplish this, the metalens must impart the phase profile φ:

$$\varphi = \frac{2\pi}{\lambda_0}\left(L_{chief} - L_{sl} - L_{lf}\right) \quad (1)$$

to null optical path length differences, where L_{sl}, L_{lf} and L_{chief} are point source-to-lens, lens-to-focal point, and chief ray (the shortest) optical path lengths, respectively, at the design wavelength λ_0 = 1.31 μm (Supplementary Section I). An analytic approach to calculating the required phase profile based on ray-tracing is presented in the Supplementary Section I. The chromatic dispersion of the metalens is designed such that the focal point shifts only axially (along the propagation axis) with wavelength variations. Later we show that such chromatic dispersion enables maintaining high-resolution imaging in an extended depth range.

The metalens building blocks, a-Si nanopillars, have a height of 750 nm and varying diameters to locally impart the required phase. The azimuthal symmetry of a-Si nanopillars (Figure 2c) results in a nearly polarization-independent metalens given the small range of incident angles (Supplementary Section II). This design is suitable for endoscopic optical imaging where light exiting the single mode fiber is randomly-polarized due to the constant motion of the fiber during imaging. Owing to its high refractive index and low absorption in the near-infrared region, a-Si is an ideal material for the nanopillars in order to construct high efficiency metalenses in this wavelength range. The high refractive index of a-Si allows closely-packed nanopillars that fulfill the Nyquist sampling criterion ($S < \frac{\lambda}{2\mathrm{NA}}$, NA:

numerical aperture, S: unit cell size, Figure 2c) with negligible near-field coupling. Nanopillars with power transmittance larger than 80% (Supplementary Section II) were selected in our design for high efficiency performance (Supplementary Figure S2). Figure 2d shows a scanning electron microscope (SEM) image of a metalens fabricated using the conventional top-down approach[38,39] (Methods).

Nano-optic endoscope characterization

We characterized the nano-optic endoscope analytically and experimentally. The nano-optic endoscope output beam was modeled using a Fresnel-Kirchhoff integral analysis (Supplementary Section III) and validated with the intensity profile measurements of the output beam. The imaging performance was subsequently assessed by modeling the OCT spectral interferometry using the nano-optic endoscope (Supplementary Section V) and measuring the imaging resolution and depth-of-focus using a resolution target. Detailed analytic models are presented in the Supplementary and measurements are described below.

We measured the three-dimensional intensity profile of the output beam at different wavelengths spanning from 1250 to 1370 nm (corresponding to the wavelength range of typical OCT light sources) using the setup shown in Figure S4. Figure 3a shows the nano-optic endoscope output beam profiles in the tangential plane (corresponding to the region specified with the dashed lines in Figure 2a) that are almost identical to those in the sagittal plane (Figure S6a), indicating negligible astigmatism. As expected, the focal point shifted axially with changing wavelength. Measured focal spots of the nano-optic endoscope in the lateral plane (xy-plane) shown in Figure 3b had nearly symmetric profiles with 12.7, 8.4, and 7.4 μm full-widths at half-maximum (FWHM) at 1250, 1310, and 1370 nm wavelengths, respectively. Higher numerical apertures at longer wavelengths due to the focal point axial shift give rise to a reduced focal spot size, consistent with our calculations based on the Fresnel-Kirchhoff integral analysis (Figure S3). The measured spot sizes are close to the values predicted using the Fresnel-Kirchhoff integral analysis and the diffraction limit (Figure S7).

Figure 3c and Figure S5 compare the output beam profiles of a commercial GRIN lens catheter (Dragonfly OPTIS Imaging Catheter, St. Jude Medical Inc.) and a ball lens catheter (Massachusetts General Hospital) with that of the nano-optic endoscope. Significantly larger astigmatism, gauged as the distance between focal points in the tangential and sagittal planes, was measured for the GRIN lens (410 μm) and the ball lens (722 μm) catheters compared to that of the nano-optic endoscope (22 μm). As evident in Figure 3c, the nano-optic endoscope focal spot profile was largely symmetric with appreciably smaller FWHM compared to the profiles of the GRIN lens (24 μm, 15 μm FWHMs in the focal plane) and the ball lens (11.6 μm, 35 μm FWHMs in the focal plane) catheters. It is difficult to determine the focal plane location for highly astigmatic optical beams; we chose the focal plane at the maximum intensity in our measurements. Ideally, the output beam profile of the nano-optic endoscope would be compared to that of conventional catheters of the same NA. However, the comparison is still valid given that the output beam profile of the higher NA nano-optic endoscope is of significantly higher quality despite the more noticeable effects of

aberrations for higher NA lenses. Figure S5 illustrates more detailed beam profiles of the three catheters.

OCT systems often use refractive lenses with low NAs to image samples with relatively long depth-of-focus. Chromatic dispersion of these lenses is typically insignificant. Therefore, the spectral interferometry analysis used for reconstruction of scattering amplitudes typically assumes a wavelength-independent incident beam[40,41]. When metalenses are used, this assumption is not valid since the chromatic dispersion normally follows that of diffractive optics and is therefore significant. Though there are techniques to reduce, increase, or reverse chromatic dispersion property of metalenses to suit specific applications[42–44], the effects of chromatic dispersion of the metalens must be considered in the spectral interferometry analysis. We present an analytic approach to spectral interferometry with chromatic lenses detailed in the Supplementary Section V. As summarized in Figure S8, this analysis predicts significantly larger imaging depth-of-focus for the nano-optic endoscope compared to the imaging depth-of-focus when an achromatic lens with the same NA is used. Spectral interferometry with the nano-optic endoscope uses back-scattered signals from excitation beams at different wavelengths with varying focal points due to the metalens chromatic dispersion. This gives rise to imaging with effective axially-shifted, overlapping field distributions with extended depth-of-focus that is larger than that produced by an achromatic lens (which is equivalent to a single wavelength excitation beam when determining the imaging depth-of-focus).

To experimentally measure the imaging resolution and depth-of-focus, we used a phantom comprised of a sub-wavelength gold line (width: 200 nm, height: 50 nm) on a glass substrate fabricated using electron beam lithography (Methods). The nano-optic endoscope was connected to a Fourier-domain OCT system[45,46] (details of which are provided in the Supplementary Section VI) including a Mach-Zehnder interferometer driven by a swept-source in the near infrared wavelength range (1240 to 1350 nm). Resolution in the tangential and sagittal planes was obtained by scanning the target pattern across the nano-optic endoscope output beam using an automated translational stage with the endoscope axis perpendicular and parallel to the line, respectively. Measurements were repeated multiple times for reliable evaluation of the resolution at different depth points. Figure 4a shows the measured point spread functions with smallest FWHMs of 6.37 μm (tangential) and 6.53 μm (sagittal). These values were slightly smaller than predictions likely due to small deviations from the linear response of the detector. The modulation transfer functions (MTF), the modulus of Fourier transform of the measured point spread functions, at different depth points are shown in Figure 4b. Graphs of measured FWHMs and spatial frequency at 10% modulation contrast are shown in Figure 4c. Solid lines and coloured regions represent polynomial fits to the repeated measurements and standard deviations. Comparison of the results in the tangential and sagittal planes indicates small astigmatism (22 μm) likely due to alignment imperfections during the endoscope assembly. The lateral resolution appears best at approximately 500 μm from the nano-optic endoscope outer surface (along the propagation direction), consistent with our analytic prediction. The effective depth-of-focus (the depth range in which FWHMs $< \sqrt{2}\,\mathrm{FWHM}_{\mathrm{min}}$) was 211 μm (tangential) and 315 μm (sagittal), significantly larger than that (90 μm) expected when an achromatic lens with the

same NA is used (Figure S8b). The increased imaging depth-of-focus demonstrates yet another remarkable property of the nano-optic endoscope, namely flexible chromatic dispersion that can be utilized to achieve high-resolution imaging at extended depth-of-focus. Crucially, this outcome is not feasible to realize using refractive lenses.

Nano-optic endoscope imaging

The nano-optic endoscope can be connected to standard OCT systems using a fiber optic rotary joint (FORJ) for endoscopic imaging. To demonstrate the imaging quality of the nano-optic endoscope in comparison with that of conventional OCT catheters, we performed imaging on fruit flesh (grape) and swine airways *ex vivo*. The fruit flesh exhibits fairly uniform cellular structures with small features (cellular walls) in the lateral and axial directions. Illustrated in Figure 5b, the image captured using the nano-optic endoscope is notably superior to that acquired using the ball lens catheter (Figure 5a); cellular walls are more clearly visualized and small sized cells can be identified in the magnified images obtained using the nano-optic endoscope in contrast to those of the ball lens catheter. Figure 5c,d show the comparison of the images obtained in the swine airway using a conventional ball lens catheter and the nano-optic endoscope. The clear delineation of the layers of the airway wall and the visualization of fine glands in the bronchial mucosa (arrow) further highlight the superior image quality of the nano-optic endoscope when compared to the corresponding images obtained with the conventional OCT catheter.

We tested the nano-optic endoscope in surgically resected human lung tissue specimens *ex vivo* and in the pulmonary airways of sheep *in vivo*. The Partners Human Research Committee Institutional Review Board (IRB) approved *ex vivo* imaging of human lung specimens (protocol 2010-P-002214/1) and the Institutional Animal Care and Use Committee (IACUC) at Massachusetts General Hospital approved the *in vivo* endobronchial OCT of the sheep (protocol 2014N000048).

The freshly excised lung tissue obtained from a patient with a lung nodule was inflated for imaging. OCT images of airways and alveolar structures were captured by inserting the nano-optic endoscope into the lungs both endobronchially and directly into the parenchyma. Figure 6a shows an image captured from a normal appearing airway. Features of the airway wall are clearly visible including the epithelium, basement membrane, and cartilage. Figure 6b shows a distal bronchiole through which multiple layers of small alveolar structures are visualized. In Figure 6c, obtained from regions of abnormality on OCT, fine signal void structures are visible that correspond to irregular glands indicating the presence of adenocarcinoma[47]. Though the dimensions of these irregular glands approach the lateral resolution of conventional OCT catheters, they are clearly distinguishable with the nano-optic endoscope due to its superior resolution.

For preliminary evaluation of the nano-optic endoscope performance *in vivo*, we conducted a preclinical endobronchial OCT study in living sheep. The nano-optic endoscope was inserted through an endotracheal tube into the pulmonary airways. *In vivo* endobronchial imaging was performed at multiple sites in the tracheobronchial tree. An example image is provided in Figure 6d highlighting features in the airway wall microstructure including the

epithelium, basement membrane, blood vessel, and cartilage, and of the surrounding parenchyma where alveoli are clearly observed. Artifacts due to non-uniform rotational distortion were observed in a very small number of frames and only in instances when the endoscope was subjected to sharp and highly tortuous paths. Similar artifacts are commonly observed when using conventional OCT catheters in difficult-to-reach locations. This preclinical evaluation of nano-optic endoscope indicated no significant flaws in the design for *in vivo* endoscopic imaging.

Discussion

Endoscopic OCT provides a wealth of information about the tissue sub-surface structures. However, the resolution and contrast of current endoscopic OCT catheters are not sufficient for several applications. For example in lung nodules, although endoscopic OCT is able to readily detect squamous cell carcinoma due to the presence of large (> 0.2 mm) nests of malignant cells[48], it can be challenging to accurately detect and diagnose adenocarcinoma where the characteristic atypical glandular features approach the resolution limits of such imaging systems. Improvements in the resolution and imaging depth of endoscopic OCT systems are crucial to increasing clinical utility. We speculate that the nano-optic endoscope will elevate the capabilities of endoscopic OCT in examining fine pathological changes in luminal tissue. Future clinically-oriented studies may assess this hypothesis.

The outer diameter of the fabricated nano-optic endoscope presented in this work is 2.8 mm, larger than the sizes of OCT catheters typically used for endoscopic imaging of pulmonary airways and coronary arteries. The dimensions of the current nano-optic endoscope were chosen based on the availability of off-the-shelve components and for ease of endoscope assembly. However, there is no essential limitation to further miniaturization of the nano-optic endoscope, even to sub-millimeter diameters similar to other imaging catheters.

The versatility and design flexibility of the nano-optic endoscope enable new functionalities that are unattainable using conventional catheter fabrication techniques. One such example, as demonstrated in this paper, is the ability to achieve high-resolution imaging through precise control of the phase of light to overcome spherical aberrations and astigmatism. High resolving power is among the most important advantages of optical imaging over other common medical imaging techniques such as sonography. Owing to its high quality output beam and dispersion management, our nano-optic endoscope demonstrates high-resolution endoscopic imaging *in vivo* at extended depth-of-focus.

The ability to control other properties of output light such as the polarization state enables a host of other applications, implausible to achieve using conventional catheters. Several tissues, such as smooth muscle[49], collagen, either innate or in fibrosis[50], and blood vessels[51] have constituent structures highly-organized in one particular direction. Polarization-sensitive imaging can differentiate these structures from surrounding tissue by detecting their innate birefringence and optic axis. However, determination of optic axis orientation is difficult in endoscopic imaging as the light exiting the catheter has an unknown polarization state due to fiber motion. Nano-optic endoscopes using polarization-sensitive metalenses can overcome these difficulties, enabling optical axis determination with no ambiguity. Further

extension of imaging depth-of-focus using light sources with broader bandwidths and additional manipulation of metalens chromatic dispersion is another important example. The unique properties of nano-optic endoscopes may also benefit other endoscopic optical imaging modalities such as confocal endomicroscopy for improved capabilities.

Methods

Fabrication process

The metalenses were fabricated using lithographic techniques[38,39]. A 750 nm-thick a-Si layer was deposited on a 170 μm-thick glass substrate using plasma-enhanced chemical vapor deposition (PECVD). The sample was spin-coated with a double layer of positive electron beam resist (MicroChem, PMMA495K A4 and PMMA950K A2) and an additional layer of conductive polymer (Showa Denko, ESPACER 300) to avoid charging effects during electron beam lithography (EBL). Nanopillar mask patterns were defined using EBL (Elionix, ELS-F125) followed by developing in MIBK:IPA and then deposition of a 30 nm-thick aluminum layer by thermal evaporation and lift-off. Inductively coupled plasma-reactive ion etching (ICP-RIE) was used to etch the nanopillar structures. Anisotropic etching was achieved using a mixture of SF_6 and C_4F_8. The aluminum mask was eventually removed by immersing the sample in the developer (Shipley, MF319). The overall size of the fabricated metalens was approximately 290 μm × 290 μm.

The fabrication of the resolution target included spin-coating of a 500 μm-thick quartz substrate with a positive electron beam resist layer (Zeon Chemicals, ZEP520A) and a conductive polymer layer (Showa Denko, ESPACER 300) and defining the pattern using EBL followed by deposition of a 50 nm-thick gold layer by thermal evaporation and lift-off.

OCT data processing

Structural OCT images were generated by standard processing techniques as previously described[46]. Processing includes fast Fourier transform (FFT) of the background-subtracted raw data, re-centring and zeroing the negative-portion of the data to remove depth degeneracy, and compensating dispersion and linearizing k-space mathematically. The square root of squares of signals from two polarization channels in logarithmic scale represents OCT structural images.

Data availability

The data that support the plots within this paper and other findings of this study are available from the corresponding author upon reasonable request.

Supplementary Material

Refer to Web version on PubMed Central for supplementary material.

Acknowledgments

This project was supported by funding from National Institute of Health (R01CA167827, R01HL133664 awarded to MJS), Air Force Office of Scientific Research (MURI: FA9550-14-1-0389, FA9550-16-1-0156 awarded to FC), and the LUNGevity Foundation/Upstage Lung Cancer. YWH and CWQ are supported by the National Research

Foundation, Prime Minister's Office, Singapore under its Competitive Research Program (CRP award no. NRF-CRP15-2015-03). This work was performed in part at Harvard's Center for Nanoscale Systems (CNS), a member of the National Nanotechnology Coordinated Infrastructure (NNCI), supported by the National Science Foundation (NSF) under NSF award no. 1541959. YWH thanks Yu-Cheng Chen for helpful comments and discussions.

References

1. Tearney GJ, et al. Scanning single-mode fiber optic catheter-endoscope for optical coherence tomography: erratum. Opt Lett. 21:912.1996; [PubMed: 19876201]
2. Tearney GJ, et al. In vivo endoscopic optical biopsy with optical coherence tomography. Science. 276:2037–2039.1997; [PubMed: 9197265]
3. Fujimoto JG, et al. High resolution in vivo intra-arterial imaging with optical coherence tomography. Heart. 82:128–133.1999; [PubMed: 10409522]
4. Yabushita H, et al. Characterization of human atherosclerosis by optical coherence tomography. Circulation. 106:1640–1645.2002; [PubMed: 12270856]
5. Kume T, et al. Assessment of coronary arterial thrombus by optical coherence tomography. Am J Cardiol. 97:1713–1717. DOI: 10.1016/j.amjcard.2006.01.0312006; [PubMed: 16765119]
6. Rollins AM, et al. Real-time in vivo imaging of human gastrointestinal ultrastructure by use of endoscopic optical coherence tomography with a novel efficient interferometer design. Opt Lett. 24:1358–1360.1999; [PubMed: 18079803]
7. Li XD, et al. Optical coherence tomography: advanced technology for the endoscopic imaging of Barrett's esophagus. Endoscopy. 32:921–930. DOI: 10.1055/s-2000-96262000; [PubMed: 11147939]
8. Sergeev A, et al. In vivo endoscopic OCT imaging of precancer and cancer states of human mucosa. Opt Express. 1:432–440.1997; [PubMed: 19377567]
9. Lam S, et al. In vivo optical coherence tomography imaging of preinvasive bronchial lesions. Clin Cancer Res. 14:2006–2011. DOI: 10.1158/1078-0432.CCR-07-44182008; [PubMed: 18381938]
10. Youngquist RC, Carr S, Davies DE. Optical coherence-domain reflectometry: a new optical evaluation technique. Opt Lett. 12:158–160.1987; [PubMed: 19738824]
11. Huang D, et al. Optical coherence tomography. Science. 254:1178–1181.1991; [PubMed: 1957169]
12. Fujimoto JG, et al. Femtosecond optical ranging in biological systems. Opt Lett. 11:150.1986; [PubMed: 19730562]
13. Fercher AF, Mengedoht K, Werner W. Eye-length measurement by interferometry with partially coherent light. Opt Lett. 13:186–188.1988; [PubMed: 19742022]
14. Choma M, Sarunic M, Yang C, Izatt J. Sensitivity advantage of swept source and Fourier domain optical coherence tomography. Opt Express. 11:2183–2189.2003; [PubMed: 19466106]
15. de Boer JF, et al. Improved signal-to-noise ratio in spectral-domain compared with time-domain optical coherence tomography. Opt Lett. 28:2067–2069.2003; [PubMed: 14587817]
16. Leitgeb R, Hitzenberger C, Fercher A. Performance of fourier domain vs. time domain optical coherence tomography. Opt Express. 11:889–894.2003; [PubMed: 19461802]
17. Wojtkowski M, Bajraszewski T, Targowski P, Kowalczyk A. Real-time in vivo imaging by high-speed spectral optical coherence tomography. Opt Lett. 28:1745–1747.2003; [PubMed: 14514087]
18. Yun S, Tearney G, de Boer J, Iftimia N, Bouma B. High-speed optical frequency-domain imaging. Opt Express. 11:2953–2963.2003; [PubMed: 19471415]
19. Liu L, et al. Imaging the subcellular structure of human coronary atherosclerosis using micro-optical coherence tomography. Nat Med. 17:1010–1014. DOI: 10.1038/nm.24092011; [PubMed: 21743452]
20. Spoler F, et al. Simultaneous dual-band ultra-high resolution optical coherence tomography. Opt Express. 15:10832–10841.2007; [PubMed: 19547440]
21. Cimalla P, Walther J, Mehner M, Cuevas M, Koch E. Simultaneous dual-band optical coherence tomography in the spectral domain for high resolution in vivo imaging. Opt Express. 17:19486–19500. DOI: 10.1364/OE.17.0194862009; [PubMed: 19997169]

22. Shu X, Beckmann L, Zhang H. Visible-light optical coherence tomography: a review. J Biomed Opt. 22:1–14. DOI: 10.1117/1.JBO.22.12.1217072017;
23. Kim J, et al. Endoscopic micro-optical coherence tomography with extended depth of focus using a binary phase spatial filter. Opt Lett. 42:379–382. DOI: 10.1364/OL.42.0003792017; [PubMed: 28146481]
24. Xi J, et al. Diffractive catheter for ultrahigh-resolution spectral-domain volumetric OCT imaging. Opt Lett. 39:2016–2019. DOI: 10.1364/OL.39.0020162014; [PubMed: 24686663]
25. Cui D, et al. Flexible, high-resolution micro-optical coherence tomography endobronchial probe toward in vivo imaging of cilia. Opt Lett. 42:867–870. DOI: 10.1364/OL.42.0008672017; [PubMed: 28198885]
26. Drexler W, et al. In vivo ultrahigh-resolution optical coherence tomography. Opt Lett. 24:1221–1223.1999; [PubMed: 18073990]
27. Standish BA, et al. In vivo endoscopic multi-beam optical coherence tomography. Phys Med Biol. 55:615–622. DOI: 10.1088/0031-9155/55/3/0042010; [PubMed: 20071753]
28. Singh K, Yamada D, Tearney G. Astigmatism corrected common path probe for optical coherence tomography. Lasers Surg Med. 49:312–318. DOI: 10.1002/lsm.225542017; [PubMed: 27490964]
29. Fang Q, et al. Ultrahigh-resolution optical coherence elastography through a micro-endoscope: towards in vivo imaging of cellular-scale mechanics. Biomed Opt Express. 8:5127–5138. DOI: 10.1364/BOE.8.0051272017; [PubMed: 29188108]
30. Shishkov, M; Bouma, BE; Tearney, GJ. Systme and method for optical coherence imaging. US Patent. 20060067620A1. 2006.
31. Ohmi S, et al. Gradient-index rod lens made by a double ion-exchange process. Appl Opt. 27:496–499. DOI: 10.1364/AO.27.0004961988; [PubMed: 20523629]
32. Khorasaninejad M, Capasso F. Metalenses: Versatile multifunctional photonic components. Science. 3582017;
33. Yu N, et al. Light propagation with phase discontinuities: generalized laws of reflection and refraction. Science. 334:333–337. DOI: 10.1126/science.12107132011; [PubMed: 21885733]
34. Khorasaninejad M, et al. Metalenses at visible wavelengths: Diffraction-limited focusing and subwavelength resolution imaging. Science. 352:1190–1194. DOI: 10.1126/science.aaf66442016; [PubMed: 27257251]
35. Huang YW, et al. Aluminum plasmonic multicolor meta-hologram. Nano Lett. 15:3122–3127. DOI: 10.1021/acs.nanolett.5b001842015; [PubMed: 25844757]
36. Balthasar Mueller JP, Rubin NA, Devlin RC, Groever B, Capasso F. Metasurface Polarization Optics: Independent Phase Control of Arbitrary Orthogonal States of Polarization. Phys Rev Lett. 118:113901.2017; [PubMed: 28368630]
37. Ralston TS, Marks DL, Carney PS, Boppart SA. Interferometric synthetic aperture microscopy. Nat Phys. 3:129–134. DOI: 10.1038/nphys5142007; [PubMed: 25635181]
38. Khorasaninejad M, Crozier KB. Silicon nanofin grating as a miniature chirality-distinguishing beam-splitter. Nat Commun. 5:5386.2014; [PubMed: 25388102]
39. Khorasaninejad M, Capasso F. Broadband Multifunctional Efficient Meta-Gratings Based on Dielectric Waveguide Phase Shifters. Nano Lett. 15:6709–6715. DOI: 10.1021/acs.nanolett.5b025242015; [PubMed: 26372331]
40. Fercher AF, Hitzenberger CK, Kamp G, El-Zaiat SY. Measurement of intraocular distances by backscattering spectral interferometry. Opt Comm. 117:43–48.1995;
41. Ha Usler G, Lindner MW. “Coherence radar” and “spectral radar”-new tools for dermatological diagnosis. J Biomed Opt. 3:21–31. DOI: 10.1117/1.4298991998; [PubMed: 23015002]
42. Khorasaninejad M, Chen WT, Oh J, Capasso F. Super-Dispersive Off-Axis Meta-Lenses for Compact High Resolution Spectroscopy. Nano Lett. 16:3732–3737. DOI: 10.1021/acs.nanolett.6b010972016; [PubMed: 27119987]
43. Khorasaninejad M, et al. Achromatic Metasurface Lens at Telecommunication Wavelengths. Nano Lett. 15:5358–5362. DOI: 10.1021/acs.nanolett.5b017272015; [PubMed: 26168329]

44. Khorasaninejad M, et al. Achromatic Metalens over 60 nm Bandwidth in the Visible and Metalens with Reverse Chromatic Dispersion. Nano Lett. 17:1819–1824. DOI: 10.1021/acs.nanolett.6b051372017; [PubMed: 28125234]
45. Yun SH, et al. Comprehensive volumetric optical microscopy in vivo. Nat Med. 12:1429–1433. DOI: 10.1038/nm14502006; [PubMed: 17115049]
46. Yun S, Tearney G, de Boer J, Bouma B. Removing the depth-degeneracy in optical frequency domain imaging with frequency shifting. Opt Express. 12:4822–4828.2004; [PubMed: 19484034]
47. Hariri LP, et al. Toward the guidance of transbronchial biopsy: identifying pulmonary nodules with optical coherence tomography. Chest. 144:1261–1268. DOI: 10.1378/chest.13-05342013; [PubMed: 23828441]
48. Hariri LP, et al. Seeing beyond the bronchoscope to increase the diagnostic yield of bronchoscopic biopsy. American journal of respiratory and critical care medicine. 187:125–129. DOI: 10.1164/rccm.201208-1483OE2013; [PubMed: 23322794]
49. Adams DC, et al. Birefringence microscopy platform for assessing airway smooth muscle structure and function in vivo. Sci Transl Med. 8:359ra131.2016;
50. Hariri LP, et al. Endobronchial Optical Coherence Tomography for Low-risk Microscopic Assessment and Diagnosis of Idiopathic Pulmonary Fibrosis In Vivo. Am J Respir Crit Care Med. 2017
51. Nadkarni SK, et al. Measurement of collagen and smooth muscle cell content in atherosclerotic plaques using polarization-sensitive optical coherence tomography. J Am Coll Cardiol. 49:1474–1481. DOI: 10.1016/j.jacc.2006.11.0402007; [PubMed: 17397678]

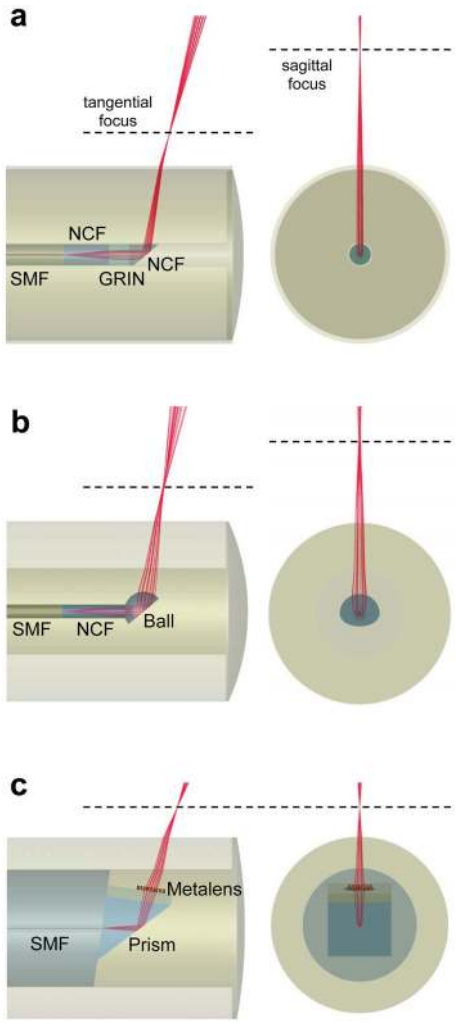

Figure 1. Endoscopic OCT catheter designs

a, **b**, Schematics of standard graded-index (GRIN) lens (**a**) and ball lens (**b**) OCT catheters. The output beams of these catheters (**a**, **b**) suffer from astigmatism primarily due to the presence of the cylindrical outer protective sheath with asymmetric curvatures in the transverse plane. **c**, Schematic of our nano-optic endoscope that uses a metalens to achieve near diffraction-limited focusing. SMF: single-mode fiber; NCF: no-core fiber.

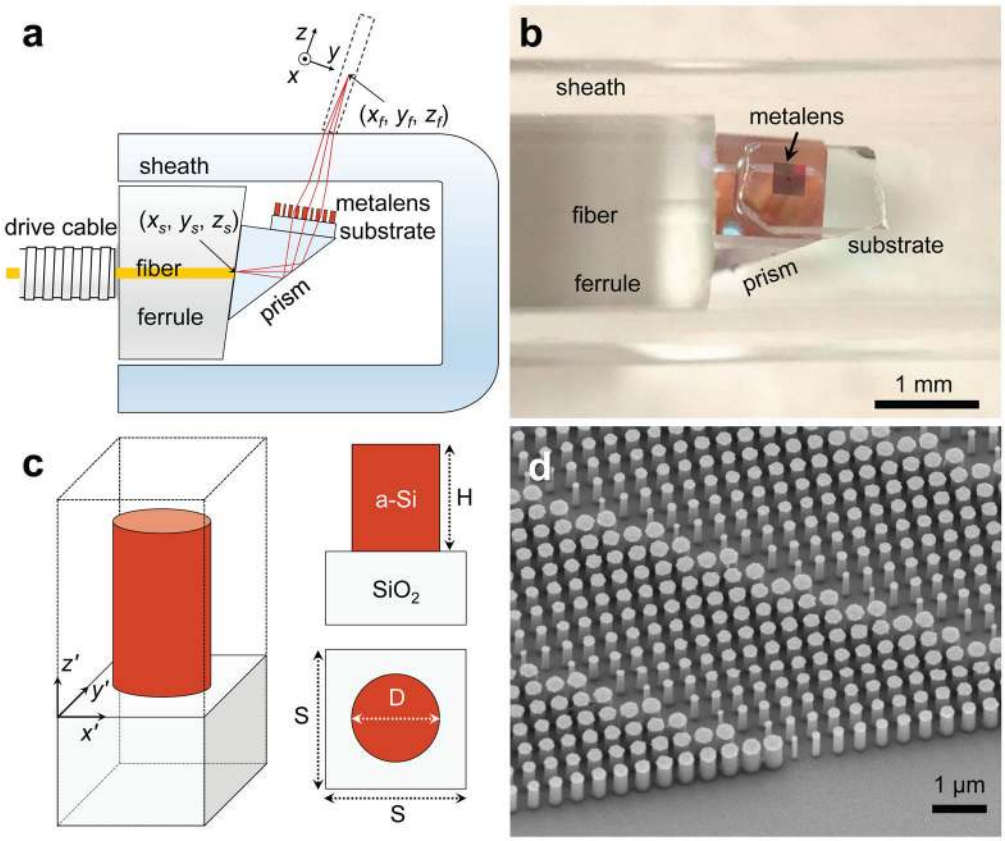

Figure 2. Nano-optic endoscope design and fabrication

a, Schematic of the nano-optic endoscope. The metalens was designed to image a point source at (x_s, y_s, z_s) to a diffraction-limited spot at (x_f, y_f, z_f) with working distance WD = 0.5 mm. **b**, Photographic image of the distal end of the nano-optic endoscope. **c**, Schematic of an individual metalens building block consisting of an amorphous silicon (a-Si) nanopillar on a glass substrate. The nanopillars have height H = 750 nm and are arranged in a square lattice with unit cell size S = 400 nm. Phase imparted by a nanopillar is controlled by its diameter (D). **d**, Scanning electron micrograph image of a portion of a fabricated metalens.

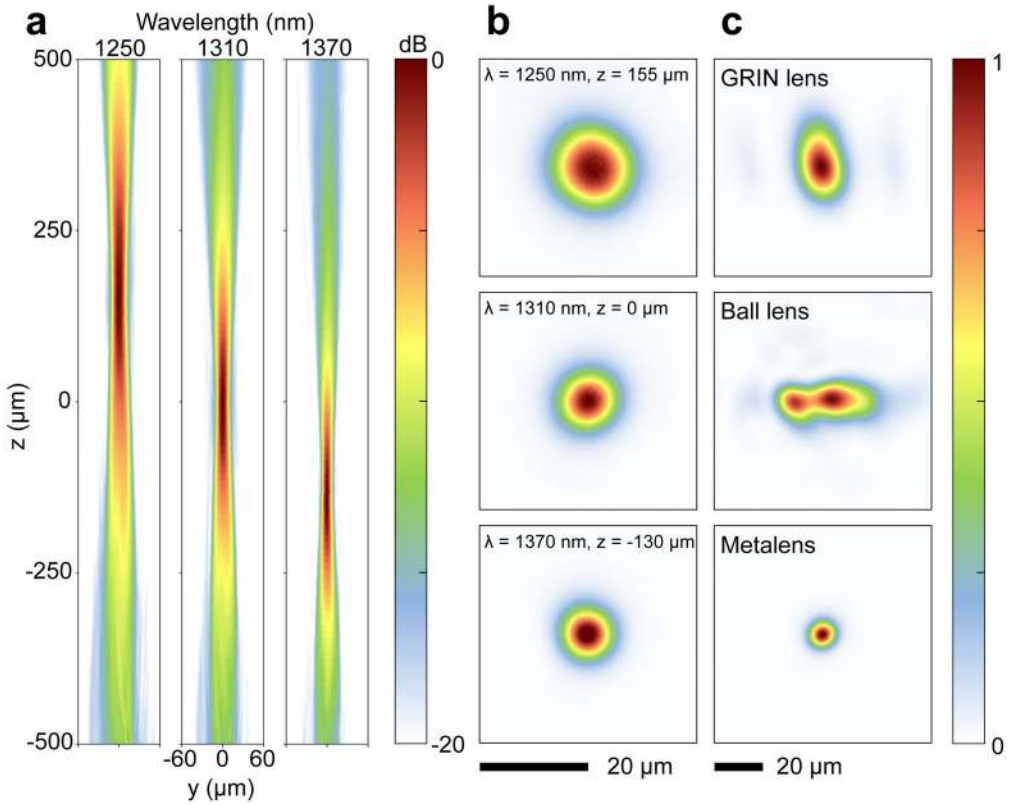

Figure 3. Optical characterization of the nano-optic endoscope and conventional OCT catheters

a, Measured intensity distribution of the nano-optic endoscope along the propagation direction in the *yz*-plane (coordinates shown in Figure 2a) at λ = 1250, 1310, and 1370 nm. **b**, Focal spot profiles of the nano-optic endoscope at corresponding wavelengths. **c**, Focal spot profiles of a graded-index (GRIN) OCT catheter, a ball lens OCT catheter, and the nano-optic endoscope at 1310 nm wavelength. The incorporation of the metalens as the focusing element enables tighter focus with negligible astigmatism.

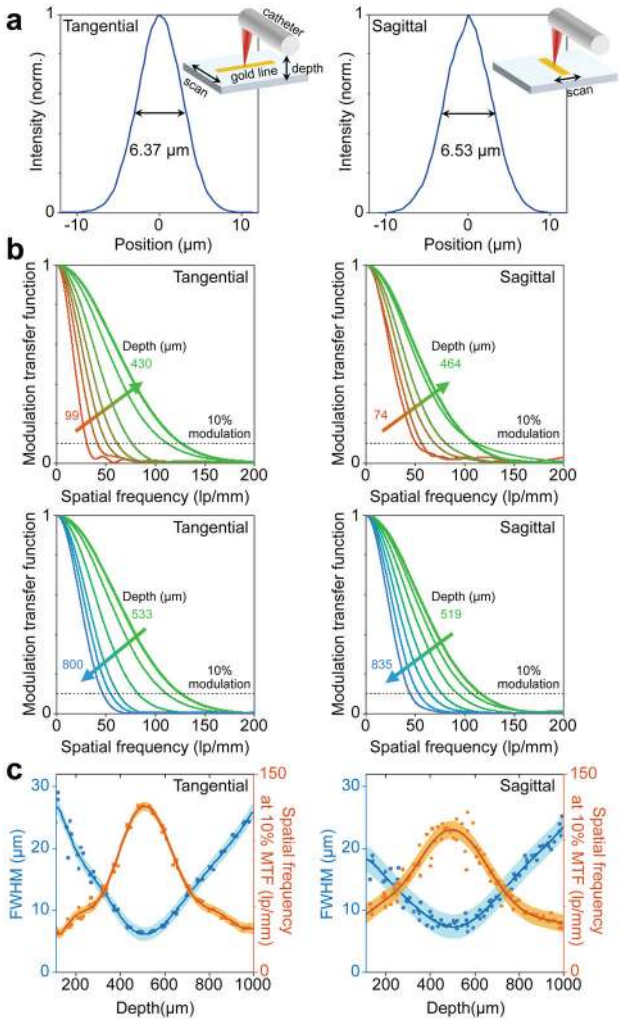

Figure 4. Resolution measurements of the nano-optic endoscope

a, Measured profiles of resolution target with the smallest full-widths at half maximum (FWHM) in the tangential and sagittal planes. **b**, Measured modulation transfer functions at different depth points in the tangential and sagittal planes. **c**, FWHM and spatial frequency at 10% modulation contrast with respect to the depth in the tangential and sagittal planes. Coloured regions and solid lines indicate standard deviations and polynomial fits to the repeated (n = 5) measurements, respectively.

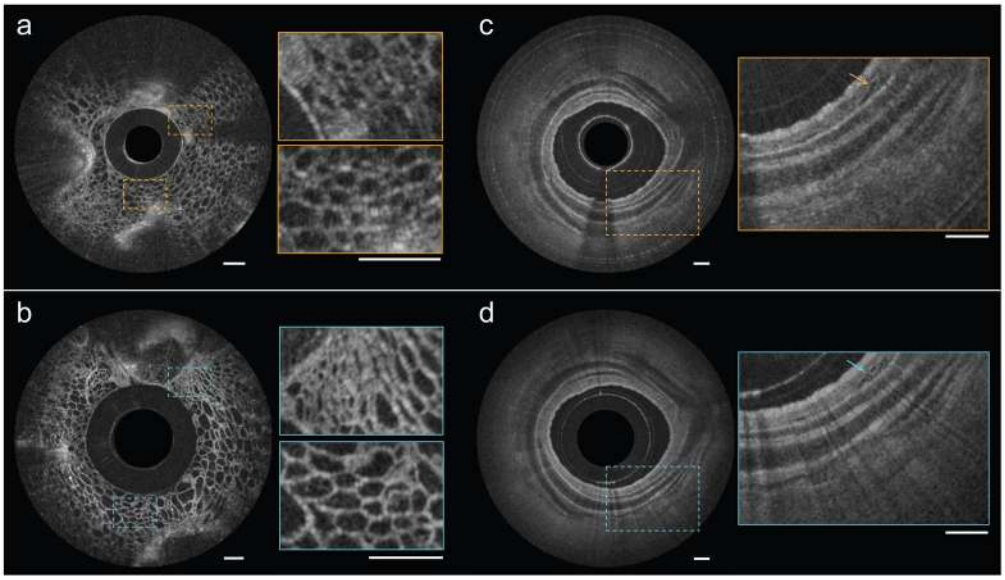

Figure 5. Comparison of OCT images obtained using the nano-optic endoscope and a conventional OCT catheter

OCT images of fruit flesh (grape) obtained using a ball lens catheter (**a**) and the nano-optic endoscope (**b**). *Ex vivo* images of swine airway using a ball lens catheter (**c**) and the nano-optic endoscope (**d**). Arrows indicate fine glands in bronchial mucosa. All scale bars are 500 μm.

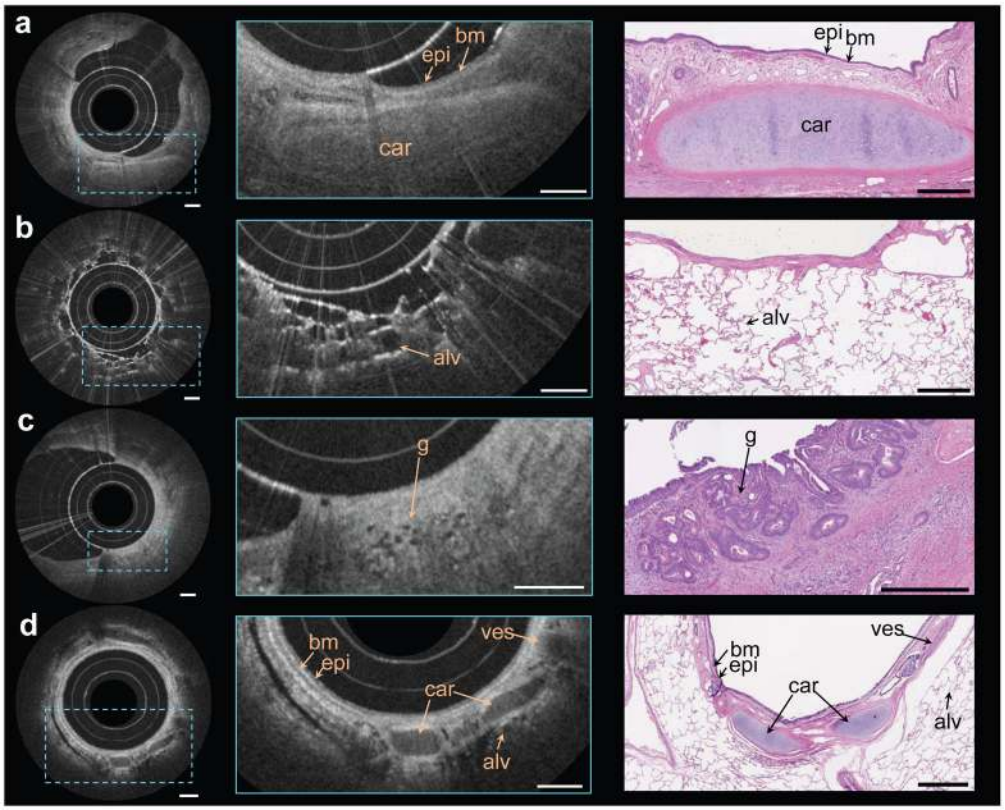

Figure 6. *In vivo* and *ex vivo* endoscopic OCT using the nano-optic endoscope

a–**d** Endoscopic imaging of *ex vivo* human lung resections (**a**, **b**, **c**) and *in vivo* in the upper airways of sheep (**d**) using the nano-optic endoscope. Structural features of lung tissue were clearly visible in the magnified OCT images (centre column) including moderately scattering epithelium (epi), highly scattering basement membrane (bm), cartilage (car), blood vessel (ves), and alveoli (alv). Fine features, including the small irregular glands (g), the hallmark of adenocarcinoma, can be discerned. Representative histological images are provided in the right column. All scale bars are 500 μm.